Growth of vertically aligned nanowires in metal–oxide nanocomposites: kinetic Monte-Carlo modeling versus experiments

M. Hennes, V. Schuler, X. Weng, J. Buchwald, D. Demaille, Y. Zheng, F. Vidal

Journal Name

ARTICLE TYPE

Cite this: DOI: 10.1039/xxxxxxxxxx

Growth of vertically aligned nanowires in metal – oxide nanocomposites: Kinetic Monte-Carlo modeling *versus* experiments

M. Hennes,*‡[a] V. Schuler,‡[a] X. Weng,[a] J. Buchwald,[b] D. Demaille,[a] Y. Zheng[a] and F. Vidal*[a]

Received Date
Accepted Date

DOI: 10.1039/xxxxxxxxxx

www.rsc.org/journalname

We employ kinetic Monte-Carlo simulations to study the growth process of metal – oxide nanocomposites obtained *via* sequential pulsed laser deposition. Using Ni – $SrTiO_3$ as a model system, we reduce the complexity of the computational problem by choosing a coarse-grained approach mapping Sr, Ti and O atoms onto a single effective STO pseudo-atom species. With this *Ansatz*, we scrutinize the kinetics of the sequential synthesis process, governed by alternating deposition and relaxation steps, and analyze the self-organization propensity of Ni atoms into straight vertically aligned nanowires embedded in the surrounding STO matrix. We finally compare the predictions of our binary toy model with experiments and demonstrate that our computational approach captures fundamental aspects of self-assembled nanowire synthesis. Despite its simplicity, our modeling strategy successfully describes the impact of relevant parameters, like concentration or laser frequency, on the final nanoarchitecture of metal – oxide thin films grown via pulsed laser deposition.

1 Introduction

Vertically aligned metal – ceramic nanocomposites constitute a new material class characterized by the presence of metallic nanopillars embedded in a planar oxide matrix. As a consequence of their very large heterointerface as well as their anisotropic optical, magnetic and electrical properties, these hybrid structures can be considered promising candidates for technological applications in various fields ranging from plasmonics [1,2], spintronics [3] and catalysis [4] to ultrahigh density magnetic data storage [5,6].

For development of novel vertical nanocomposites, pulsed laser deposition (PLD) synthesis relying on self-organized growth has recently emerged as a novel technique, complementing conventional methods such as electrodeposition into prestructured templates [7–9]. On the one hand, self-assembly based procedures avoid cumbersome intermediate steps and permit to create arrays of ultrathin nanowires ($d < 5$ nm) with extremely high densities ($\rho > 10^{11}/\mathrm{cm}^2$). On the other hand, the metallic and oxide phases exhibit vertical epitaxial coupling, which is especially interesting when dealing with magnetic nanocomposites. Indeed, pronounced differences in lattice parameters between the matrix and the metallic nanoinclusions paves the way for magnetic anisotropy control via strain engineering [10] and synthesis of artificial multiferroics [11,12].

Obviously, the design of application-optimized composites requires precise control of their nanoarchitecture. The inter-wire spacing must be carefully tuned to achieve a compromise between high areal density and detrimental magnetic dipole-dipole interactions. At the same time, accurate adjustment of the nanowire radius is required, as it intrinsically limits the thermal stability of the encoded magnetic information. In addition, it also plays a crucial role in determining the final strain state of the nanowire [10].

A variety of parameters influencing the structure of vertically aligned nanocomposites has been identified in recent years. The temperature [13] and deposition frequency [14] were for example found to have a strong impact on the diameter of embedded nanocolumns grown via PLD. However, while the number of experimental studies dealing with magnetic metal – oxide VANs increases steadily [14–19], there has been little progress in the theoretical description of the growth process. The details of the mechanisms giving rise to self-organized, matrix-embedded wire arrays remain poorly understood.

In the present work, we therefore scrutinize synthesis of hybrid metal-oxide thin films from an experimental, as well as from a theoretical perspective. On the one hand, we use a lattice kinetic Monte-Carlo (KMC) *Ansatz* to analyze the growth of hybrid Ni – $SrTiO_3$ (Ni – STO) thin films. By choosing a coarse-grained

[a] *Sorbonne Université, CNRS, Institut des NanoSciences de Paris, INSP, F-75005 Paris, France*
[b] *Institute for Materials Science and Max Bergmann Center of Biomaterials, Dresden University of Technology, 01062 Dresden, Germany*
‡ These authors contributed equally to this work.

approach, which only takes Ni and matrix pseudo-atoms into consideration, we obtain a simple and powerful toy-model which allows for an atomic-scale description of the initial stages of STO-embedded Ni nanopillar growth and permits to link synthesis parameters to the final nanocomposite structure. On the other hand, we employ sequential PLD, to grow Ni – STO thin films on STO(001) substrates and compare experimental results with predictions from our simulations. In addition, we also scrutinize various related metal-perovskite nanocomposites, like Ni – $(Sr,Ba)TiO_3$ and CoNi – $(Sr,Ba)TiO_3$ and analyze to what extent the present simulation results can be generalized to these material systems.

The paper is structured as follows: We start by giving a detailed presentation of our KMC simulation results. We then turn to our experimental findings and discuss these results with respect to our KMC data and available literature results. We finally close with a summary and outlook.

2 Results and discussion

2.1 KMC simulation results

Sequential PLD is based on laser ablation using a set of interchangeable targets, resulting in alternate deposition of different atomic species and ensuing thin film growth on a substrate placed in vicinity of the plasma plume[17,19] (Fig. 1a). In the present simulation study, we focus on Ni – $SrTiO_3$ nanocomposite synthesis relying on alternating addition of matrix constituents to the substrate surface, *i.e.*, Sr, Ti and O atoms, described by a single effective matrix species (STO) in our KMC approach, and Ni atoms, respectively. A detailed description of our simulation strategy is given in the Methods part of the present paper.

Fig. 1b shows a series of representative KMC results illustrating early stage system configurations during sequential PLD-based nanocomposite growth ($T = 870\,\mathrm{K}$, $N_x \times N_y = 50 \times 50$). In this simulation, a $(18|3)$ sequence has been used, *i.e.*, 18 STO followed by 3 Ni deposition events. The system states after repetition of $N = 1, 2, 3, 5$ and 10 of these sequences are depicted in Fig. 1b(ii), (iv), (vi), (vii) and (viii) respectively. Additionally, Fig. 1b(i),(iii) and (v) show intermediate configurations during the first, second and third sequence after Ni and before STO deposition.

Closer analysis of these results allows to give a simple qualitative description of the growth process. After addition of Ni to the substrate, surface diffusion of single atoms results in formation of islands, as illustrated in Fig. 1b(i). During the subsequent steps, encompassing further relaxation due to target change induced waiting time as well as matrix atom deposition, Ostwald-ripening occurs at the surface. Small islands dissolve, releasing Ni atoms which attach to larger, energetically favored structures, as seen by comparing Fig. 1b(i) and (ii) or Fig. 1b(iii) and (iv). On the other hand, deposition of coarse-grained STO pseudo-atoms results in simultaneous matrix growth. At 870 K, Ni surface diffusion is fast enough to prevent vertical kinetic trapping, *i.e.*, covering of Ni atoms by the surrounding oxide. Successive layerwise stacking of Ni islands eventually leads to formation of straight and dense columns, buried in the surrounding STO matrix, as can be seen in Fig. 1b(viii).

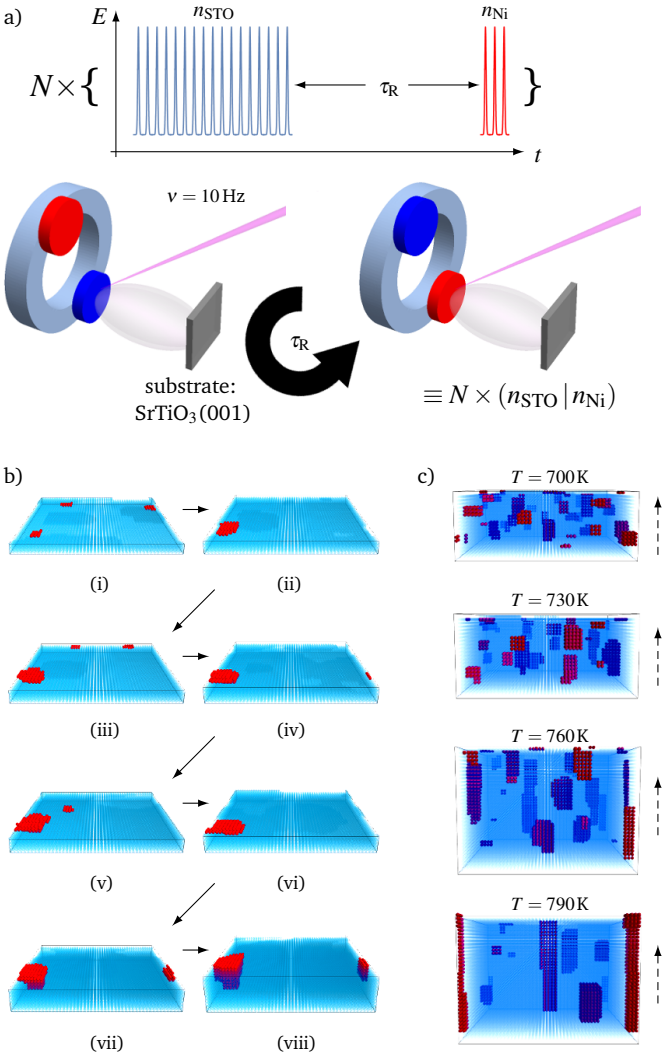

Fig. 1 a) Schematics depicting PLD-based thin film growth with sequential ablation from 2 different targets. b) Early stages of nanocomposite growth modeled with KMC, Ni atoms are shown in red, STO pseudo-atoms in blue. c) Impact of growth temperature on Ni nanoinclusion morphology (dashed arrows indicate the growth direction of the composite thin film).

As shown in Fig. 1c, temperature plays a key role during this process. Varying T from 700 K to 790 K, we observe that low temperature growth results in a cluster-like nanocomposite structure. Nanopillar formation is clearly suppressed, which can be attributed to the reduced mobility of Ni atoms. With increasing temperature, the length of the nanoinclusions increases. While at 700 K, the average metal structure height $\langle h \rangle$ equals 4.5 monolayers (ML), yielding an aspect ratio close to one, increasing T from 730 K to 760 K and 790 K results in $\langle h \rangle \approx 6.5, 8.5, 15$ ML, respectively. The transition temperature from cluster or rod-like to pure nanowire-growth with percolating metallic structures crossing the entire thin film (*i.e.*, fulfilling the condition $\langle h \rangle = \langle N_z \rangle$, $\langle N_z \rangle$ being the average thin film thickness) was determined to be $T_c \approx 820\,\mathrm{K}$ in the present simulations.

To facilitate comparison with experimental work, simulations with varying ratio of Ni to STO-atom deposition steps n_{Ni}/n_{STO}

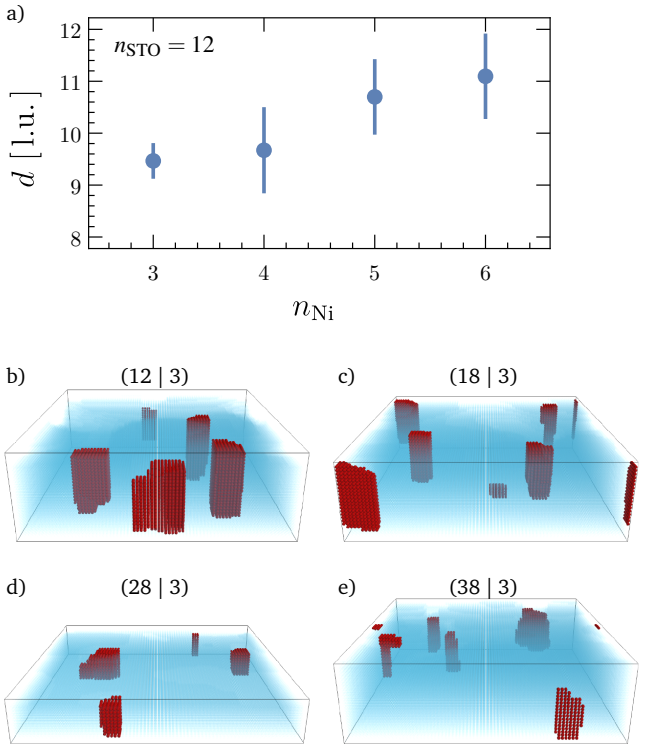

Fig. 2 Nanocomposite structure as a function of the n_{Ni}/n_{STO} ratio: a) average nanowire diameter in lattice units (l.u.) as a function of n_{Ni} ($n_{STO} = 12$) and b), c), d), e) variation of n_{STO} (keeping $n_{Ni} = 3$).

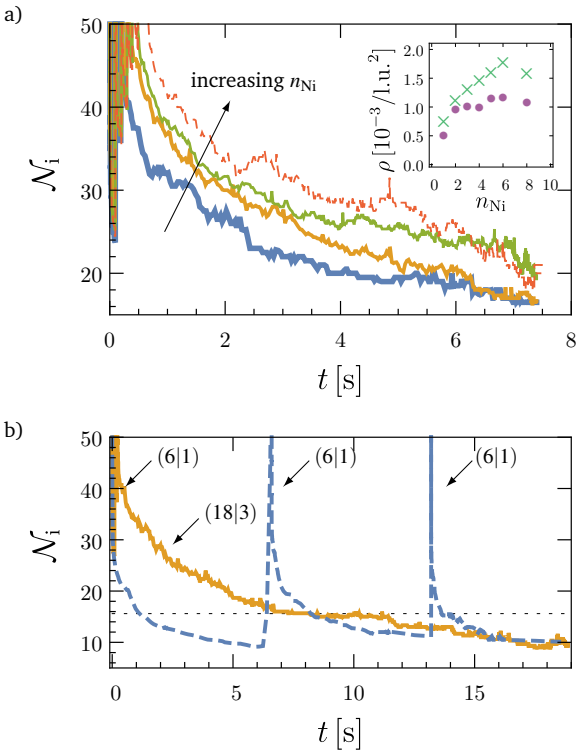

Fig. 3 Evolution of the total Ni island number $\mathcal{N}_i$ as a function of time at the surface of the growing thin film: a) for $n_{Ni} = 3$ (blue), $n_{Ni} = 4$ (orange), $n_{Ni} = 5$ (green), $n_{Ni} = 6$ (red, dashed). Inset: Island density as a function of n_{Ni} computed for $t = 3$ s (green crosses) and $t = 7.2$ s (purple dots). b) Total island number as a function of time: single (18 | 3) sequence with subsequent relaxation (orange curve), three (6 | 1) sequences (blue, dashed curve) and total island number at the end of a single (18 | 3) sequence, without additional relaxation time (black dots)

were performed, resulting in a change of the thin film composition ($T = 820$ K, $N_x \times N_y = 80 \times 80$). As exemplified in Fig. 2a, gradual increase of n_{Ni} for constant n_{STO} ($n_{STO} = 12$) resulted in a monotonic increase of the average wire diameter. In contrast, the wire density remained unaffected with average value $\langle \rho \rangle = \frac{\mathcal{N}_{nanowire}}{N_x N_y a^2} \approx 8 \pm 1 \cdot 10^{11}/\text{cm}^2$ derived from the number of nanowires $\mathcal{N}_{nanowire}$ in the simulation cell, a being the typical cubic unit lattice parameter ($a \approx a_{STO}/\sqrt{2}$). A similar behavior was obtained when simulating sequences with varying n_{STO} (while keeping $n_{Ni} = 3$), as shown in exemplary configurations in Fig. 2b,c,d,e. Despite the large variation of n_{STO}, the number of wires in the simulation cell remained constant while their diameters decreased significantly with increasing n_{STO} values.

To gain further insight into the dynamics of the initial stages of the growth process, we analyzed the evolution of the Ni island number $\mathcal{N}_i$ at the surface of the thin film during the first deposition sequence ($\nu = 10$ Hz, $T = 820$ K, $N_x \times N_y = 128 \times 128$). Fig. 3a shows $\mathcal{N}_i(t)$ calculated for various n_{Ni} values (keeping $n_{STO} = 12$). While $\mathcal{N}_i$ is clearly largest for high n_{Ni}/n_{STO} ratios, it reaches an almost constant value towards the end of the sequence, with relative differences in island number dropping below 20%. This is additionally illustrated in the inset of Fig. 3a, where the island density ρ is shown as a function of n_{Ni}. While for 7.2 s simulation time, the value of ρ saturates rapidly, it keeps growing linearly as a function of n_{Ni} when the total length of the sequence is decreased to 3 s, highlighting the intimate link between available relaxation time and final nanowire density.

The impact of Ostwald ripening on nanocomposite growth and its importance in determining the final nanocomposite architecture when using sequential PLD can further be illustrated by comparing $N_1 \times (n_{STO} \,|\, n_{Ni})$ growth protocols with multiple deposition sequences $N_2 \times (n \cdot n_{STO} \,|\, n \cdot n_{Ni})$. In our simulations $n = N_1/N_2 = 3$ was used to obtain final configurations with identical amount of Ni and STO pseudo-atoms ($\nu = 10$ Hz, $T = 820$ K, $N_x \times N_y = 80 \times 80$), therefore eliminating effects that might be attributed to a change in overall nanocomposite concentration. After deposition of 20 ML, the wire density obtained using a (6 | 1) simulation scheme was approximately equal to $4 \cdot 10^{11}/\text{cm}^2$ which is half the value resulting from (18 | 3) sequences. Considering that both systems contain the same ratio of Ni and STO pseudo-atoms, it follows that (6 | 1)-type sequences must yield larger nanowire diameters, which is what we observe in our simulations.

Again, it is instructive to analyze the number of Ni islands $\mathcal{N}_i$ present at the surface during the initial growth stages to understand how this behavior emerges from the interplay of deposition and relaxation phases. Fig. 3b shows the results of simulation runs where $\mathcal{N}_i(t)$ has been computed for a $3 \times (6 \,|\, 1)$ sequence

and its $1\times(18|3)$ counterpart ($T = 820\,\mathrm{K}$, $N_x \times N_y = 128 \times 128$). In order to obtain comparable total simulation times, the $1\times(18|3)$ sequence has been complemented by additional relaxation time. All results were averaged over five different runs, to gain better statistics. As was already observed in Fig. 3a, the island number increases dramatically immediately after deposition. Between two subsequent deposition steps, $\mathcal{N}_\mathrm{i}$ then sharply decreases as a function of time, which is due to Ni atom diffusion and island coalescence. However, the relaxation behavior of both systems differs significantly. Indeed, the larger amount of metal atoms added at once to the system during a $(18|3)$ sequence leads to a higher number of islands during early relaxation, when compared to a single $(6|1)$ sequence – in agreement with the previous part of the discussion (Fig. 3a). As a direct consequence of a larger number of target exchange moves, the total growth time resulting from a $3\times(6|1)$ protocol exceeds by far the one of its $1\times(18|3)$ counterpart. Thus, in a single $(18|3)$ sequence, the system is given significantly less time for Ostwald ripening, which eventually explains the higher amount of islands at the end of the sequence and the aforementioned difference in final nanowire densities. Allowing further relaxation after completion of a $(18|3)$ sequence (keeping the total number of atoms in the system constant) reveals that $\mathcal{N}_\mathrm{i}^{(18|3)}(3\tau^{(6|1)}) \approx \mathcal{N}_\mathrm{i}^{(6|1)}(\tau^{(6|1)})$, which suggests that the matrix atoms have only little impact on Ni island coalescence when considering sub-ML deposition.

Taken together, these findings show that sequential PLD can give rise to different growth regimes, which will depend on the specific setup design, growth protocol and nanocomposite materials: (i) short relaxation times or, equivalently, low surface mobility of the segregating metal atoms (Ni in our present study), will give rise to an increase of ρ with $n_\mathrm{metal}/n_\mathrm{oxide}$. In contrast, in a system with (ii) large relaxation times or high metal atom mobility, an increase of n_metal will result in a larger nanocolumn diameter at constant density. In addition, our modeling approach highlights that sequences of $(n\cdot n_\mathrm{metal}\,|\,n\cdot n_\mathrm{oxide})$-type can be used as a strategy to tune nanowire diameters and densities, while simultaneously keeping the metal/oxide ratio constant.

2.2 Modeling *vs.* experiments

Having presented a qualitative analysis of the main mechanisms governing nanocomposite growth, we now turn to a comparison of our KMC modeling approach with experiments. As reported in our previous studies, PLD-based sequential deposition of Ni and $SrTiO_3$ on $SrTiO_3(001)$ substrates was shown to result in phase separation and growth of vertically aligned metallic Ni nanowires [10]. In the present paper, we present additional results on Ni – $SrTiO_3$ nanocomposite synthesis and focus on the impact of concentration on the final nanowire morphology, diameters and densities. These data are complemented by experiments on Ni – (Sr,Ba)TiO_3 (Ni – SBTO) and $Co_{40}Ni_{60}$ – (Sr,Ba)TiO_3 (CoNi – SBTO) thin films in order to explore to what extent the present simulation results also apply to similar metal – perovskite material systems [19].

Fig. 4a, b, c show HR-TEM plan-views of Ni – STO samples where the growth sequence has been systematically varied. In these experiments, the number of Ni deposition steps was kept constant, while n_STO was successively doubled. As can immediately be inferred from the micrographs, the metal/oxide ratio has a strong impact on the nanowire diameter: high $n_\mathrm{Ni}/n_\mathrm{STO}$ ratios clearly give rise to larger nanowires. We thus retrieve the trend that was identified in our KMC simulations, where the nanowire diameter grew monotonically as a function of $n_\mathrm{Ni}/n_\mathrm{STO}$. We also find good qualitative agreement concerning the shape of the embedded nanowires. Indeed, their straight morphology and complete absence of kinks or pronounced diameter modulations, is perfectly compatible with our KMC predictions (Fig.4d).

In addition to the nanowire size and morphology, we determined the porosity of each sample, defined as the

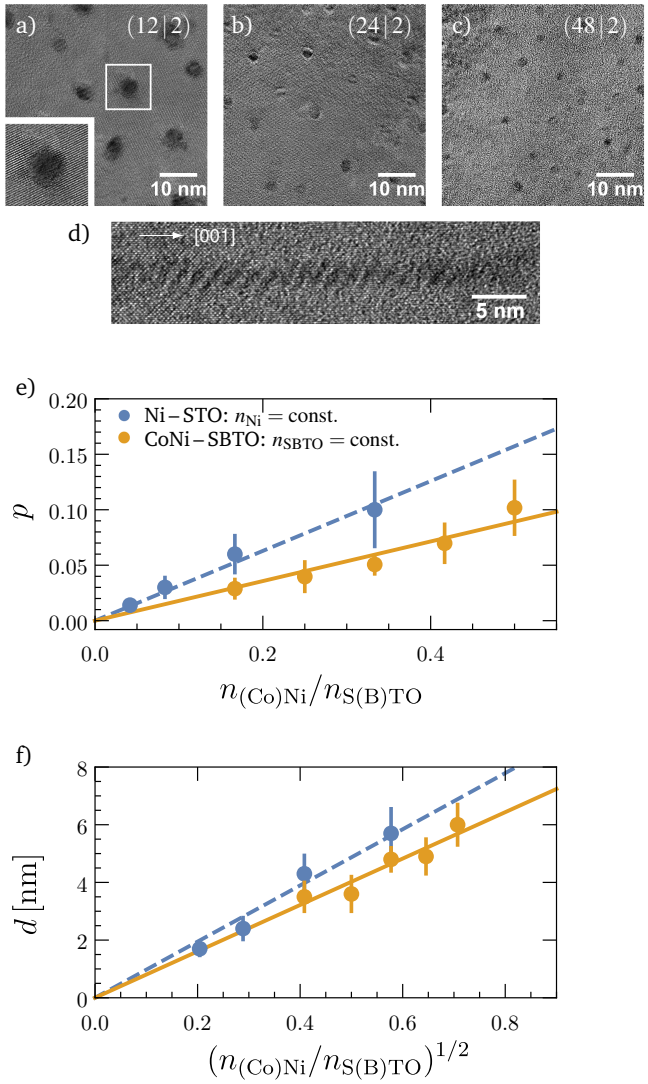

Fig. 4 Metal–oxide nanocomposites grown via sequential PLD: a), b), c) HR-TEM plan-views of Ni – STO nanocomposites. d) Cross sectional HR-TEM micrograph of a Ni–SBTO thin film with a buried Ni nanowire giving rise to characteristic Moiré patterns. e) porosity and f) nanowire diameter as a function of $n_\mathrm{(Co)Ni}/n_\mathrm{S(B)TO}$ and $(n_\mathrm{(Co)Ni}/n_\mathrm{S(B)TO})^{1/2}$ as well as linear fits (Ni: blue, dashed line, CoNi: orange, solid line).

nanowire/matrix surface ratio in a projection perpendicular to the thin film surface. The results are plotted in Fig. 4e. We observe a similar behavior in Ni–STO as well as CoNi–SBTO systems, a linear increase of p with $n_{(Co)Ni}/n_{S(B)TO}$ characterizing pure columnar growth. As the porosity is directly linked to the nanowire areal number density ρ and radius r *via* $p = \rho\pi r^2$, we conclude that the nanowire diameter must obey $d \propto \rho^{-1/2}(n_{(Co)Ni}/n_{S(B)TO})^{1/2}$. For the synthesis protocols used in our experiments, our KMC simulations predict an almost constant nanowire density for all Ni–STO samples ($\langle\rho\rangle \approx 8 \cdot 10^{11}\mathrm{cm}^{-2}$). This is indeed what we observe in our experiments, in Ni–STO ($\langle\rho\rangle = 5.1 \pm 1.1 \cdot 10^{11}\mathrm{cm}^{-2}$) but also in CoNi–SBTO thin films ($\langle\rho\rangle = 3.4 \pm 0.4 \cdot 10^{11}\mathrm{cm}^{-2}$), which display a very similar behavior. As a result, a simple relationship linking concentration and nanowire diameter is eventually obtained: $d \propto (n_{(Co)Ni}/n_{S(B)TO})^{1/2}$, as shown Fig. 4f.

Although our modeling approach is focused on metal–oxide nanocomposite growth, it is interesting to compare the present results with earlier studies on oxide–oxide nanocolumnar thin films, where experimental information concerning the relationship between final nanoarchitecture and growth conditions is available. In $BiFeO_3-CoFe_2O_4$ thin film synthesis[13], the diameter of embedded $CoFe_2O_4$ structures was found linked to the growth rate $\tilde{\nu}$ *via* $d \propto \tilde{\nu}^{-1/2}$. This was also reported in Sm-doped CeO_2–$SrTiO_3$ vertical heteroepitaxial nanocomposites[20]. In the present study, the same result is retrieved in a growth regime where ρ is independent of $n_{(Co)Ni}/n_{S(B)TO}$. Indeed, when keeping $n_{(Co)Ni}$ fixed, $d \propto \tilde{\nu}^{-1/2}$ immediately follows from $d \propto \rho^{-1/2}(n_{CoNi}/n_{S(B)TO})^{1/2}$ when thin film growth is dominated by S(B)TO atom addition ($p \ll 1$). However, as has been put forward in an earlier part of this work, it must be emphasized that very different growth conditions can be encountered. For example, self-organization of Co wires in CeO_2 via sequential PLD resulted in nanocomposites with constant wire diameter and decreasing wire density when increasing the number of shots on the CeO_2 target[21], which might suggest a significantly different surface mobility of Co atoms on CeO_2 surfaces. The scaling relations identified in the present metal–perovskite systems, which also apply to some extent to selected oxide–oxide nanocomposites, will thus not necessarily remain valid in other types of nanocolumnar metal–oxide thin films.

Another difficulty encountered when trying to compare the present results with earlier work on vertically aligned nanocomposites arises from the fact that most studies described in literature rely on single target PLD-growth for nanocomposite synthesis[4,14,18]. To close this gap, we conducted additional simulations where Ni and STO pseudo-atoms were deposited simultaneously and not sequentially. Fig. 5a and 5b show exemplary results from simulations performed with varying n_{Ni}/n_{STO} ratios ($\nu = 10\,\mathrm{Hz}$, $T = 820\,\mathrm{K}$, $N_x \times N_y = 80 \times 80$). At first sight, the system exhibits a behavior which appears to correspond to our findings based on sequential synthesis. We indeed observe growth of nanowires with rather straight morphology and our results demonstrate that an increase of n_{Ni}/n_{STO} yields a larger average nanowire diameter. However, careful analysis of the data indicates that the wire density does not stay constant when changing n_{Ni}/n_{STO}. While the small system sizes used in our simulations impede an improvement of the statistics and make a reliable analysis of nanowire densities difficult, we found evidence supporting an increase of ρ with the amount of Ni atoms in the system. This might be traced back to shorter relaxation steps, when compared to sequential PLD, as has been discussed in a previous part of this paper. Indeed, without any intermediate relaxation, as introduced artificially during sequential growth, the laser frequency ν imposes the typical time scale during which the system evolves with constant number of Ni atoms. A variation of ν should therefore have a measurable impact on the synthesis process and the final structure of the nanocomposite.

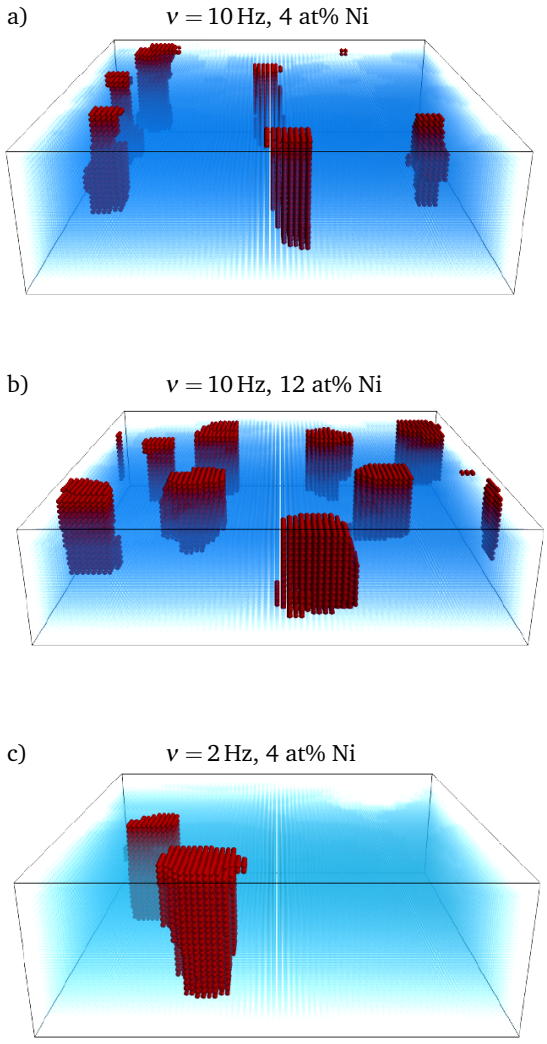

Fig. 5 KMC simulation of nanocomposite growth from a single target: a) at $\nu = 10\,\mathrm{Hz}$ and 4 at% Ni in the nanocomposite, b) changing the Ni/STO ratio and finally, c) reducing the laser frequency to $\nu = 2\,\mathrm{Hz}$.

To test this hypothesis, we performed various simulations based on a single target growth scheme, reducing the frequency by a factor of 5. Fig. 5c shows a representative configuration resulting from simulation runs using $\nu = 2$ Hz ($T = 820\,\mathrm{K}$, $N_x \times N_y =$

80×80). As can clearly be observed, the laser frequency severely influences the resulting nanocomposites, yielding a significant increase of the wire diameter when lowering the frequency. This finding has very recently been reported in PLD-based growth of $Co-BaZrO_3$ thin films, where the laser frequency was used to tune the magnetic properties of the resulting thin films[14]. However, our simulations also indicate that a reduction of the frequency leads to a concomitant reduction of ρ. The present work demonstrates how the introduction of additional relaxation steps (inherent to sequential growth) can be used as a simple, yet powerful strategy to circumvent these problems and decouple ρ and $\langle d \rangle$ to eventually achieve an increased control of the final nanocomposite architecture.

3 Conclusions

In this study, we presented a coarse-grained lattice KMC approach which we employed to model sequential PLD growth of metal–oxide nanocomposites. Using $Ni-SrTiO_3$ as a model system, we analyzed the initial stages of growth and were able to identify key parameters affecting the final nano-architecture of the thin film. We showed that synthesis at lower temperatures resulted in phase separated composites characterized by small Ni nanoinclusions, with aspect ratio close to one, embedded in a STO matrix. Increasing the growth temperature favorized the growth of rods and, above 820 K, eventually resulted in nanowires spanning from the bottom of the thin film to its surface. We highlighted that systematically raising n_{Ni}/n_{STO} during each cycle, yielded an increased average nanowire diameter, while the overall wire density remained constant. Careful analysis of the growth procedure allowed to show how this behavior emerged from the subtle interplay of deposition and relaxation phases. Control of the relaxation time between deposition steps was thus identified as a key requirement to accurately tune the nanowire size and density. On an atomic level, our KMC approach is far from grasping the details and subtleties of metal–oxide interactions (*e.g.* strain induced effects, surface reconstructions, defects) and we did not strive for an exhaustive quantitative treatment of the problem. However, when comparing our findings with experimental results, we observed reasonable qualitative agreement with respect to the evolution of wire density and diameter upon changes in the synthesis parameters. We therefore conclude that, despite its shortcomings, our simulation approach provides a robust scheme to understand key issues affecting nanowire self-assembly and lays the groundwork for future studies aiming at a more elaborate description of the growth of metal – oxide nanocomposites.

4 Methods

Kinetic Monte-Carlo

KMC results presented in this work rely on an implementation of the residence time algorithm proposed by Bortz[22]. To simplify computations, $Ni-SrTiO_3$ nanocomposite growth resulting from sequential addition of Sr, Ti, O and Ni atoms to the surface of the thin film was approximated by a binary system, composed of Ni and STO pseudo-atoms atoms only. All simulations were performed on a rigid lattice with $N_x \times N_y$ sites and in plane periodic boundary conditions. The lattice was chosen as simple cubic, *i.e.* each effective atom having four in plane nearest neighbors, which reflects the fourfold symmetry of (001) $SrTiO_3$ planes when the composite is growing in [001] direction. Differences in lattice parameters and resulting misfit strains were neglected.

Only two major processes were included into our KMC simulations: (i) simultaneous addition of N_{Ni} or N_{STO} atoms to the surface of the growing thin film and (ii) their subsequent diffusion. Desorption of the deposited objects as well as chemical reactions were not taken into consideration. Regarding (i), the number of deposited atoms was varied with simulation cell size and adapted such as to closely match experimental conditions (during PLD growth, approximately 25 deposition events were required on average to achieve single ML deposition). Additionally, we took into account the different deposition yields from single pulses on the two targets: laser ablation on $SrTiO_3$ was found to generate roughly four times the number of Ni atoms. Atom deposition was treated as a process where (x,y) coordinates on the surface were chosen at random. With respect to (ii), we only included surface diffusion in our simulations. Every atom could jump from its current position to one of the four nearest neighbor adjacent sites. Volume diffusion was neglected: any atom at position (x,y,z) covered by another atom at $(x,y,z+1)$ remained immobile. However, vertical or "climbing"-moves were explicitely incorporated, with atoms at position (x,y,z) allowed to step up to position $(x,y+1,z+1)$ whenever an atom was present at position $(x,y+1,z)$.

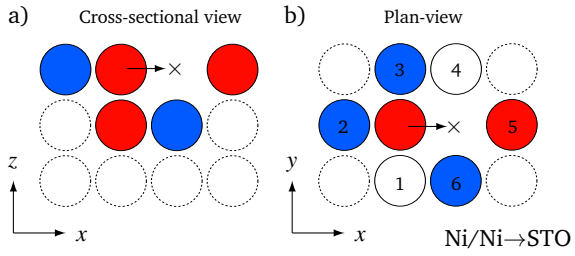

Fig. 6 Determination of energy barriers using an exemplary diffusion move: a) a Ni atom on a top Ni site diffuses to a top STO site (Ni/Ni→STO), the final position is marked with a cross for better visibility (Ni atoms are shown in red, STO pseudo-atoms in blue). In the present model, only neighbor atom sites marked with solid contour line are relevant for energy barrier height determination. b) Corrections ΔE to the energy barrier arise from in-plane neighbors at initial and final sites (labeled 1, 2, 3 and 4, 5, 6, respectively).

The jump of an effective atom of type l at lattice site (x_i,y_i,z_i) to one of its nearest neighbors at (x_f,y_f,z_f) is a thermally activated event. Transition state theory allows to compute transition rates from knowledge of energy barriers separating initial and final states *via*

$$k = k_0 e^{-E_B/k_B T} \tag{1}$$

with k_B, T, k_0 and E_B being the Boltzmann constant, temperature, jump frequency ($k_0 \approx 10^{13}$ Hz) and barrier energy, respectively. In a binary system, diffusion of single atoms on a planar

Table 1 Energy barriers and next neighbor energy values used for KMC simulations as well as literature references and DFT results from the present study (highlighted with a star ⋆). All values are given in eV.

	KMC		Literature values & DFT
$E_{\mathrm{Ni/Ni\to Ni}}$	0.65		0.645 [24], 0.631 [25]
$E_{\mathrm{Ni/Ni\to STO}}$	1.3		-
$E_{\mathrm{Ni/STO\to STO}}$	1.0	Ni / SrO	0.67⋆
		Ni / TiO_2	2.37⋆, 1.8⋆, 1.4⋆, 0.55⋆
$E_{\mathrm{STO/STO\to STO}}$	0.5		0.6 [26], 0.97 [27], 0.3 [28]
		O/SrO:	0.53, 0.64 [29], 0.81 [30]
		O/TiO_2:	0.68 [30]
		Sr/SrO:	0.77, 0.83 [29]
$\Delta E_{\mathrm{Ni-Ni}}$	0.35		0.325 [24], 0.383 [25]
$\Delta E_{\mathrm{Ni-STO}}$	0.1		-
$\Delta E_{\mathrm{STO-STO}}$	0.7		0.5 [28]

surface then requires determination of 2^3 parameters $E_{l/k\to j}$, with atomic species k at $(x_i, y_i, z_i - 1)$ and j at $(x_f, y_f, z_f - 1)$, as depicted in Fig. 6. Additionally, nearest neighbors in plane impact the barrier energy. In the present work, we modeled this behavior by using simple pair interaction terms [23], summed over the atom types at nearest neighbor sites

$$\Delta E_l = \sum n_m^{(i)} \Delta E_{lm} - \sum n_m^{(f)} \Delta E_{lm} \qquad (2)$$

Here, $n_m^{(i)}$ is the number of next neighbors of type m ($m \equiv$ Ni, STO) surrounding the starting position of the diffusional move in plane (sites 1, 2, 3 in Fig. 6), $n_m^{(f)}$ indicates the number of m-type next neighbors around the arrival site (4, 5, 6 in Fig. 6). The final barrier energy of a diffusing l-type atom thus reads, $E_B = E_{l/k\to j} + \Delta E_l$. Energies $E_{l/k\to j}$ and in-plane corrections ΔE_{lm} used in the present work as an input for KMC simulations are listed in Table 1.

Diffusion barrier heights relating to pure Ni – Ni and effective STO – STO interactions were directly deduced from literature. $E_{\mathrm{STO/STO\to STO}}$ determination remained somewhat arbitrary, due to the coarse-grained nature of our approach (resulting from mapping of Sr, Ti and O atoms onto a single STO species). However, available data revealed little spread and no pronounced dependency on the surface termination was reported. To reduce the number of free parameters and further simplify the calculations, we assigned the same energy to all STO pseudo-atom moves: $E_{\mathrm{STO/STO\to STO}} = E_{\mathrm{STO/STO\to Ni}} = E_{\mathrm{STO/Ni\to Ni}} = E_{\mathrm{STO/Ni\to STO}}$. Due to lack of literature values, Ni – $SrTiO_3$ interaction energies had to be assessed by performing preliminary KMC and DFT calculations. Based on experimental evidence reporting 3D island creation for Ni deposited on $SrTiO_3$ [31] (reflecting the high interface energy of the system), we determined $E_{\mathrm{Ni/Ni\to STO}}$ by performing KMC simulations for different values of this parameter and scrutinized the onset of isolated vertical Ni structures growth (islands with more than 1 ML thickness) when depositing sub-monolayer quantities of Ni on the surface. For determination of $E_{\mathrm{Ni/STO\to STO}}$, DFT calculations were undertaken, which will be described in detail in the next paragraph. We used $E_{\mathrm{Ni/STO\to STO}} = E_{\mathrm{Ni/STO\to Ni}}$, a similar simplification as the one employed for STO pseudo-atom diffusion. Finally, $\Delta E_{\mathrm{Ni-STO}}$ was determined by considering the requirements $\Delta E_{\mathrm{Ni-STO}} < \Delta E_{\mathrm{Ni-Ni}}$ and $\Delta E_{\mathrm{Ni-STO}} < \Delta E_{\mathrm{STO-STO}}$ to induce segregation in our binary model system. We therefore chose a rather small, yet non-zero in-plane interaction energy $E = 0.1\,\mathrm{eV}$ between Ni and STO pseudo-atoms.

Density functional theory

We employed density functional theory (DFT) calculations to identify Ni-addatom minimum energy sites and minimum energy paths on planar $SrTiO_3(001)$ surfaces. All calculations were performed using the Quantum Espresso software package [32] with ultrasoft pseudopotentials and PBE exchange correlation [33,34]. The kinetic energy cutoff was set to 35 Ry while the charge density cutoff was chosen fourteen times as high. The integration over the Brillouin zone was performed with a $3 \times 3 \times 1$ Monkhorst-Pack mesh [35]. The simulation cell employed in our study consisted of a single STO-cube with volume $3a_0^{\mathrm{STO}} \times 3a_0^{\mathrm{STO}} \times 3a_0^{\mathrm{STO}}$ ($a_0^{\mathrm{STO}} = 3.923\,\text{Å}$) and periodic boundary conditions in plane, combined with $3a_0$ vacuum inserted in z to create (001) surfaces (Fig. 7a and Fig. 7c). Plan-views of the different surface configurations scrutinized in the present work are shown in Fig. 7b and Fig. 7d. In a first computational step, all $SrTiO_3$ surfaces were structurally relaxed using the BFGS algorithm [36–39] until the force components on every atom were less than $10^{-4}\,\mathrm{Ry}/a_0$ and changes in the total energy were found smaller than $10^{-5}\,\mathrm{Ry}$. In a second step, we placed a single Ni atom at various canonical positions (*e.g.* on top of oxygen atoms or at bridge positions between two oxygen atoms). Keeping the bottom layer fixed, we then performed a geometry optimization by minimizing the energy of the system within a spin-polarized calculation scheme. To compute the height of the energy barriers, we used a climbing image nudge elastic band (NEB) simulation scheme [40]. The simulations were considered to be converged, when the abolute value of the force orthogonal to the path was lower than 0.05 eV/Å.

In Fig. 7e and Fig. 7f the lowest energy paths for Ni migration on the SrO- and TiO_2-terminated STO(001) surfaces are shown. For every NEB simulation, we used five images, which were connected by appropriate polynomial interpolation. For Ni migration on SrO terminated surfaces, we found one major saddle point ($E = 0.67\,\mathrm{eV}$), located half way between two slightly asymmetric top-O positions, as shown in Fig. 7g. A small intermediate energy barrier is considered of minor importance for the present surface diffusion analysis. For Ni diffusion on TiO_2 terminated site, we identified different paths, which are shown in Fig. 7h-k. The first path connects two global minima corresponding to a Ni atom located in a FH-oxygen position (Fig. 7h) with a barrier height of $E = 2.37\,\mathrm{eV}$. A second competing path with almost identical maximum saddle point energy is shown in (Fig. 7i-j). Here, the Ni atom crosses a first saddle point ($E = 1.4\,\mathrm{eV}$) reaching a local minimum configuration with twofold oxygen coordination (Fig. 7i5 and Fig. 7j1'), where one of the O-atoms is slightly pushed out of the surface plane. In a second step, the Ni atom leaves this twofold coordinated site and moves into a top-O configuration, a diffusional step with energy barrier height of $E = 1.8\,\mathrm{eV}$ (the over-

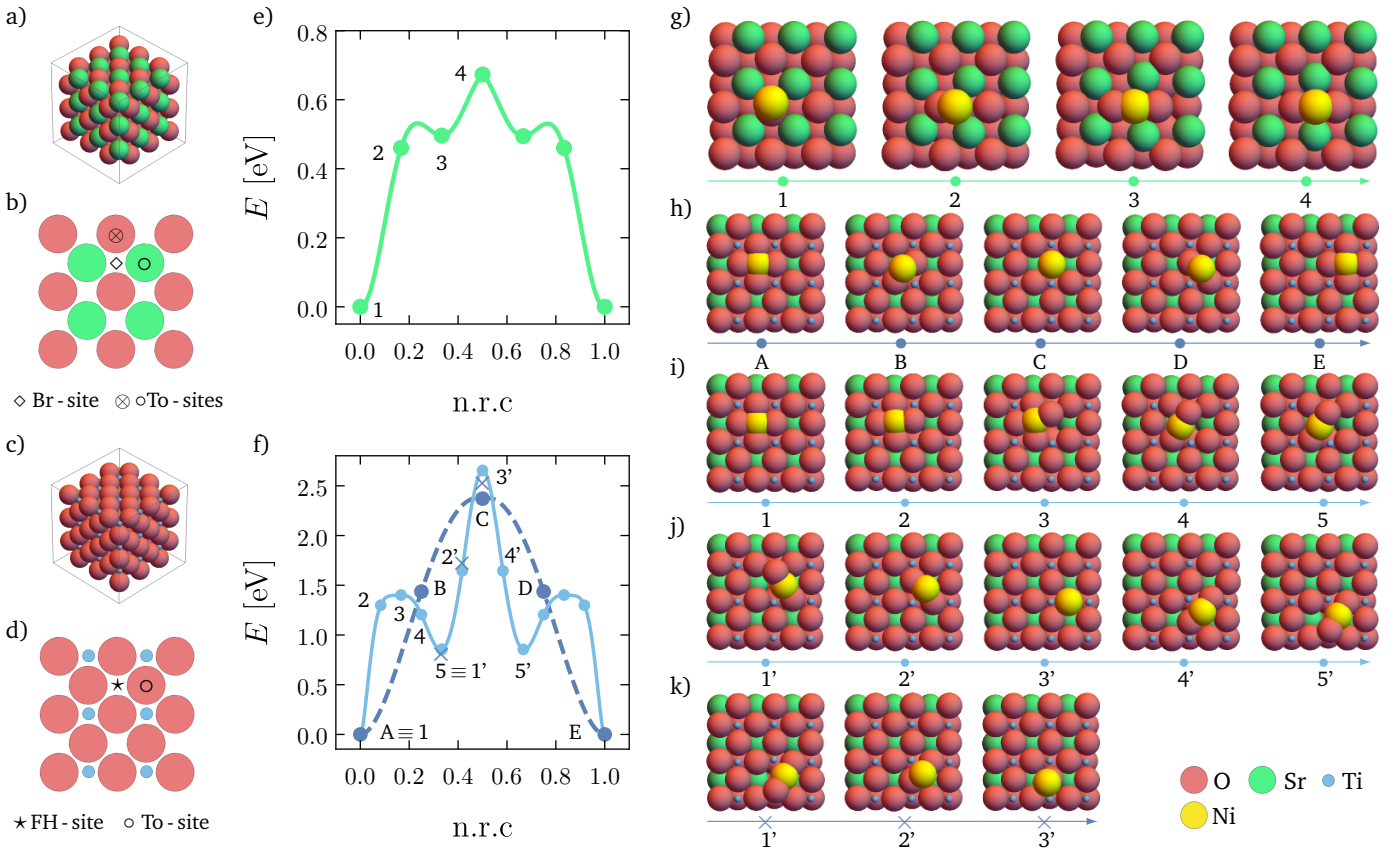

Fig. 7 Summary of the DFT results obtained in the present study. a) Simulation cell employed for analysis of diffusion on SrO-terminated surfaces and b) plan-view of a SrO-terminated (A-site) surface. c) Simulation cell employed for analysis of diffusion on TiO_2-terminated surfaces and d) plan-view of a TiO_2-terminated (B-site) surface. Energy of the system as a function of the normalized reaction coordinate (n.r.c) for Ni diffusion on e) SrO-terminated and f) TiO_2-terminated STO(001) surfaces. g) Diffusion path of a Ni atom on A-site surfaces (energies labeled $1 \rightarrow 2 \rightarrow 3 \rightarrow 4$ in e) from left to right). On TiO_2 terminated surfaces, different paths with similar saddle point energies were identified: h) Diffusion from FH to FH sites, corresponding energy curve labeled dark blue (dashed) in f). i) and j) show Ni diffusion paths from FH to FH sites, with an intermediate local minimum resulting from an oxygen atom "lift-up move", corresponding energies labeled in f) $1 \rightarrow 2 \rightarrow 3 \rightarrow 4 \rightarrow 5$ (for the path shown in i), from left to right) and $1' \rightarrow 2' \rightarrow 3' \rightarrow 4' \rightarrow 5'$ (for the path shown in j), from left to right). Finally, k) alternative oxygen "lift-up move" characterized by a similar saddle point energy (labeled in f) with blue crosses).

all height with respect to the FH position amounts to $E = 2.65\,\text{eV}$). The final move towards the global minimum eventually requires crossing a smaller barrier with $E = 0.55\,\text{eV}$. In addition to moves connecting global minima, we checked that Ni atoms can also evolve between local minima (Fig. 7i1' and Fig. 7j5'), which involves a slightly modified diffusional path, with similar energy barrier of 1.77 eV (Fig. 7k).

Due to mapping of Sr, Ti and O onto a single pseudo-atom species, our KMC model is not able to differentiate between A- and B-site terminations. Considering that SrO surfaces were shown to be thermodynamically more stable than their TiO_2 counterparts[41,42], and in absence of any experimental evidence describing immobilization or trapping of single Ni atoms on the surface during growth, we eventually chose $E_{\text{Ni/STO}\rightarrow\text{STO}} = 1\,\text{eV}$, a parameter value close to DFT results describing Ni diffusion on a SrO-terminated surface.

Thin film synthesis

$Ni-SrTiO_3$, $Ni-(Sr,Ba)TiO_3$ as well as $CoNi-(Sr,Ba)TiO_3$ nanocomposites were grown *via* sequential pulsed laser deposition using a qudrupled Nd:YAG laser with $\lambda = 266\,\text{nm}$ (Quantel) operated at 10 Hz with typical fluences $1\,\text{J/cm}^2 < F < 3\,\text{J/cm}^2$. For sample synthesis, NiO, CoO and $SrTiO_3$ targets were used in a reductive environment ($P < 10^{-6}$ mbar). Atomic deposition was carried out on $SrTiO_3(001)$ substrates (SurfaceNet GmbH) heated to $T \approx 650^{\circ}\text{C}$. Compositional tuning of the nanocomposite was achieved by changing the ratio of laser shots on the NiO, CoO and $SrTiO_3$ target, respectively. The notation $N\times(n_{\text{STO}}\,|\,n_{\text{(Co)Ni}})$ is used in the present work to describe series of N sequences with $n_{\text{(Co)Ni}}$ shots on the NiO and CoO targets followed by n_{STO} shots on the $SrTiO_3$ target (see [17,19] for a detailed description). A typical time of $\tau_R = 3\,\text{s}$ was required to switch between the targets. After completing nanocomposite growth, the surface of the thin film was eventually covered with an additional matrix layer of several nm thickness to prevent oxidation under ambient conditions. High-Resolution Transmission Electron Microscopy data were ac-

quired with a JEOL JEM 2100F equipped with a field-emission gun (FEG) and operated at 200 kV.

Conflicts of interest

There are no conflicts of interest to declare

Acknowledgements

We are indebted to F. Breton for skillful help with the PLD setup, J.-M. Guigner of IMPMC (CNRS-UPMC) is acknowledged for providing access to the TEM facilities. M. Hennes acknowledges financial support from the French Embassy in Berlin ("Service pour la Science et la Technologie") and Campus France. We thank the Center for Information Services and High Performance Computing (ZIH), TU Dresden for providing computing time. This work has been funded in parts by the LabEx Matisse (projects ANR-11-IDEX-0004-02/10-LABX-0067 - MATISSE)

References

1 A. V. Kabashin, P. Evans, S. Pastkovsky, W. Hendren, G. A. Wurtz, R. Atkinson, R. Pollard, V. A. Podolskiy, and A. V. Zayats. Plasmonic nanorod metamaterials for biosensing. *Nat Mater*, 8(11):867–871, 2009.

2 Jie Yao, Zhaowei Liu, Yongmin Liu, Yuan Wang, Cheng Sun, Guy Bartal, Angelica M. Stacy, and Xiang Zhang. Optical negative refraction in bulk metamaterials of nanowires. *Science*, 321(5891):930–930, 2008.

3 Luc Piraux, Krystel Renard, Raphael Guillemet, Stefan Mátéfi-Tempfli, Mária Mátéfi-Tempfli, Vlad Andrei Antohe, Stéphane Fusil, Karim Bouzehouane, and Vincent Cros. Template-grown NiFe/Cu/NiFe nanowires for spin transfer devices. *Nano Letters*, 7(9):2563–2567, 2007.

4 Seiji Kawasaki, Ryota Takahashi, Takahisa Yamamoto, Masaki Kobayashi, Hiroshi Kumigashira, Jun Yoshinobu, Fumio Komori, Akihiko Kudo, and Mikk Lippmaa. Photoelectrochemical water splitting enhanced by self-assembled metal nanopillars embedded in an oxide semiconductor photoelectrode. *Nature Communications*, 7:11818 EP –, 2016.

5 Shaoguang Yang, Hao Zhu, Dongliang Yu, Zhiqiang Jin, Shaolong Tang, and Youwei Du. Preparation and magnetic property of Fe nanowire array. *Journal of Magnetism and Magnetic Materials*, 222(1-2):97 – 100, 2000.

6 D.H Qin, M Lu, and H.L Li. Magnetic force microscopy of magnetic domain structure in highly ordered co nanowire arrays. *Chemical Physics Letters*, 350(1-2):51 – 56, 2001.

7 Satoshi Kawai and Ryuzo Ueda. Magnetic properties of anodic oxide coatings on aluminum containing electrodeposited Co and Co-Ni. *Journal of The Electrochemical Society*, 122(1):32–36, 1975.

8 Hideki Masuda and Kenji Fukuda. Ordered metal nanohole arrays made by a two-step replication of honeycomb structures of anodic alumina. *Science*, 268(5216):1466–1468, 1995.

9 A Fert and L Piraux. Magnetic nanowires. *Journal of Magnetism and Magnetic Materials*, 200(1-3):338 – 358, 1999.

10 Vivien Schuler, Francisco Javier Bonilla, Dominique Demaille, Alessandro Coati, Alina Vlad, Yves Garreau, Michèle Sauvage-Simkin, Anastasiia Novikova, Emiliano Fonda, Sarah Hidki, Victor Etgens, Franck Vidal, and Yunlin Zheng. Huge metastable axial strain in ultrathin heteroepitaxial vertically aligned nanowires. *Nano Research*, 8(6):1964–1974, 2015.

11 Xiefei Yao, Jing Ma, Yuanhua Lin, Ce-wen Nan, and Jinxing Zhang. Magnetoelectric coupling across the interface of multiferroic nanocomposites. *Science China Materials*, 58(2):143–155, 2015.

12 Jijie Huang, Judith L. MacManus-Driscoll, and Haiyan Wang. New epitaxy paradigm in epitaxial self-assembled oxide vertically aligned nanocomposite thin films. *Journal of Materials Research*, 32:1–13, 2017.

13 H. Zheng, F. Straub, Q. Zhan, P.-L. Yang, W.-K. Hsieh, F. Zavaliche, Y.-H. Chu, U. Dahmen, and R. Ramesh. Self-assembled growth of $BiFeO_3$-$CoFe_2O_4$ nanostructures. *Advanced Materials*, 18(20):2747–2752, 2006.

14 Jijie Huang, Leigang Li, Ping Lu, Zhimin Qi, Xing Sun, Xinghang Zhang, and Haiyan Wang. Self-assembled Co-$BaZrO_3$ nanocomposite thin films with ultra-fine vertically aligned Co nanopillars. *Nanoscale*, 9:7970–7976, 2017.

15 L. Mohaddes-Ardabili, H. Zheng, S. B. Ogale, B. Hannoyer, W. Tian, J. Wang, S. E. Lofland, S. R. Shinde, T. Zhao, Y. Jia, L. Salamanca-Riba, D. G. Schlom, M. Wuttig, and R. Ramesh. Self-assembled single-crystal ferromagnetic iron nanowires formed by decomposition. *Nature Materials*, 3:533, 2004.

16 F. Vidal, Y. Zheng, P. Schio, F. J. Bonilla, M. Barturen, J. Milano, D. Demaille, E. Fonda, A. J. A. de Oliveira, and V. H. Etgens. Mechanism of localization of the magnetization reversal in 3 nm wide Co nanowires. *Phys. Rev. Lett.*, 109:117205, 2012.

17 Francisco Javier Bonilla, Anastasiia Novikova, Franck Vidal, Yunlin Zheng, Emiliano Fonda, Dominique Demaille, Vivien Schuler, Alessandro Coati, Alina Vlad, Yves Garreau, Michèle Sauvage Simkin, Yves Dumont, Sarah Hidki, and Victor Etgens. Combinatorial growth and anisotropy control of self-assembled epitaxial ultrathin alloy nanowires. *ACS Nano*, 7(5):4022–4029, 2013.

18 Qing Su, Wenrui Zhang, Ping Lu, Shumin Fang, Fauzia Khatkhatay, Jie Jian, Leigang Li, Fanglin Chen, Xinghang Zhang, Judith L. MacManus-Driscoll, Aiping Chen, Quanxi Jia, and Haiyan Wang. Self-assembled magnetic metallic nanopillars in ceramic matrix with anisotropic magnetic and electrical transport properties. *ACS Applied Materials & Interfaces*, 8(31):20283–20291, 2016.

19 V Schuler, J Milano, A Coati, A Vlad, M Sauvage-Simkin, Y Garreau, D Demaille, S Hidki, A Novikova, E Fonda, Y Zheng, and F Vidal. Growth and magnetic properties of vertically aligned epitaxial CoNi nanowires in (Sr, Ba)TiO_3 with diameters in the 1.8 - 6 nm range. *Nanotechnology*, 27(49):495601, 2016.

20 Seungho Cho, Chao Yun, Stefan Tappertzhofen, Ahmed Kursumovic, Shinbuhm Lee, Ping Lu, Quanxi Jia, Meng Fan, Jie Jian, Haiyan Wang, Stephan Hofmann, and Judith L. MacManus-Driscoll. Self-assembled oxide films with tailored

nanoscale ionic and electronic channels for controlled resistive switching. *Nat. Commun.*, 7:12373 EP –, 2016.

21 V. Schuler. *Self-assembled ferromagnetic nanowires embedded in an oxide matrix: growth mechanisms, vertical epitaxy and magnetic properties*. PhD thesis, Université Pierre et Marie Curie.

22 A.B. Bortz, M.H. Kalos, and J.L. Lebowitz. A new algorithm for Monte Carlo simulation of ising spin systems. *Journal of Computational Physics*, 17(1):10 – 18, 1975.

23 I. Mouton, E. Talbot, C. Pareige, R. Lardé, and D. Blavette. The early stage of formation of self-organized nanocolumns in thin films: Monte Carlo simulations versus atomic-scale observations in Ge-Mn. *Journal of Applied Physics*, 115(5):053515, 2014.

24 Hanoch Mehl, Ofer Biham, Itay Furman, and Majid Karimi. Models for adatom diffusion on fcc (001) metal surfaces. *Phys. Rev. B*, 60:2106–2116, 1999.

25 J. Merikoski, I. Vattulainen, J. Heinonen, and T. Ala-Nissila. Effect of kinks and concerted diffusion mechanisms on mass transport and growth on stepped metal surfaces. *Surface Science*, 387(1):167 – 182, 1997.

26 Aaron Fleet, Darren Dale, A. R. Woll, Y. Suzuki, and J. D. Brock. Multiple time scales in diffraction measurements of diffusive surface relaxation. *Phys. Rev. Lett.*, 96:055508, 2006.

27 J. D. Ferguson, G. Arikan, D. S. Dale, A. R. Woll, and J. D. Brock. Measurements of surface diffusivity and coarsening during pulsed laser deposition. *Phys. Rev. Lett.*, 103:256103, 2009.

28 Qinglei Zhang, Jiliang Zhu, Junzhe Tan, Guanglong Yu, Jiagang Wu, Jianguo Zhu, and Dingquan Xiao. Monte Carlo simulation of the growth of $SrTiO_3$ thin film with molecular source. *Vacuum*, 81(4):539 – 544, 2006.

29 Minki Hong, Jennifer L. Wohlwend, Rakesh K. Behera, Simon R. Phillpot, Susan B. Sinnott, and Blas P. Uberuaga. Surface diffusion on $SrTiO_3$ (100): A temperature accelerated dynamics and first principles study. *Surface Science*, 617:237 – 241, 2013.

30 Hannes Guhl, Wolfram Miller, and Karsten Reuter. Oxygen adatoms at $SrTiO_3$(001): A density-functional theory study. *Surface Science*, 604(3-4):372 – 376, 2010.

31 Jingyu Sun, Chen Wu, Fabien Silly, Antal A. Koos, Frank Dillon, Nicole Grobert, and Martin R. Castell. Controlled growth of Ni nanocrystals on $SrTiO_3$ and their application in the catalytic synthesis of carbon nanotubes. *Chem. Commun.*, 49:3748–3750, 2013.

32 Paolo Giannozzi, Stefano Baroni, Nicola Bonini, Matteo Calandra, Roberto Car, Carlo Cavazzoni, Davide Ceresoli, Guido L Chiarotti, Matteo Cococcioni, Ismaila Dabo, Andrea Dal Corso, Stefano de Gironcoli, Stefano Fabris, Guido Fratesi, Ralph Gebauer, Uwe Gerstmann, Christos Gougoussis, Anton Kokalj, Michele Lazzeri, Layla Martin-Samos, Nicola Marzari, Francesco Mauri, Riccardo Mazzarello, Stefano Paolini, Alfredo Pasquarello, Lorenzo Paulatto, Carlo Sbraccia, Sandro Scandolo, Gabriele Sclauzero, Ari P Seitsonen, Alexander Smogunov, Paolo Umari, and Renata M Wentzcovitch. Quantum espresso: a modular and open-source software project for quantum simulations of materials. *Journal of Physics: Condensed Matter*, 21(39):395502, 2009.

33 John P. Perdew, Kieron Burke, and Matthias Ernzerhof. Generalized gradient approximation made simple. *Phys. Rev. Lett.*, 77:3865–3868, 1996.

34 Yingkai Zhang and Weitao Yang. Comment on "generalized gradient approximation made simple". *Phys. Rev. Lett.*, 80:890–890, 1998.

35 Hendrik J Monkhorst and James D Pack. Special points for Brillouin-zone integrations. *Physical review B*, 13(12):5188, 1976.

36 C. G. Broyden. The convergence of a class of double-rank minimization algorithms 1. general considerations. *IMA Journal of Applied Mathematics*, 6(1):76, 1970.

37 R. Fletcher. A new approach to variable metric algorithms. *The Computer Journal*, 13(3):317, 1970.

38 Donald Goldfarb. A family of variable-metric methods derived by variational means. *Mathematics of computation*, 24(109):23–26, 1970.

39 David F Shanno. Conditioning of quasi-newton methods for function minimization. *Mathematics of computation*, 24(111):647–656, 1970.

40 Graeme Henkelman, Blas P. Uberuaga, and Hannes Jónsson. A climbing image nudged elastic band method for finding saddle points and minimum energy paths. *The Journal of Chemical Physics*, 113(22):9901–9904, 2000.

41 A.A. Demkov. Investigating alternative gate dielectrics: A theoretical approach. *physica status solidi (b)*, 226(1):57–67, 2001.

42 Xiaodong Zhang and Alexander A. Demkov. Steps on the (001) SrTiO3 surface. *Journal of Vacuum Science and Technology B: Microelectronics and Nanometer Structures*, 20(4):1664–1670, 7 2002.